MASTER DEGREE IN
Nanostructured Materials
for Nanotechnology Applications
University of Zaragoza

Final Master Project

Universidad Zaragoza

EELS Plasmonic Studies on Gold Nanostructures

J. Carlos Grimalt Escarabajal

Supervisor: Dr. R. Arenal

Academic year 2019/20

LMA
LABORATORIO DE MICROSCOPIAS AVANZADAS

Facultad de Ciencias
Universidad Zaragoza

Instituto Universitario de Investigación
en Nanociencia de Aragón
Universidad Zaragoza

1. Abstract

In this Final Master Project, plasmonic studies on gold-based nanostructures have been carried out by using electron energy loss spectroscopy in a monochromated transmission electron microscope. The optical response of these metallic nanoparticles and their applications are important research and technological fields in nanoscience. The theory behind plasmonics, concerning surface plasmons in relation with size, shape, and composition of the nanostructure, and how their resonance modes can be measured and interpreted using electron energy loss spectroscopy is overviewed. A methodology developed recently by the research group has been used to extract this plasmonic information from the low-loss region in detail, and five different nanostructures have been chosen from different samples synthetized with gold as the main component for that purpose. Compositional analyses of the samples have been developed via energy dispersive X-rays spectroscopy. Finally, a critical interpretation and discussion of the results have been realized using other plasmonic studies as references to conclude with detailed relations between size, shape and composition of the nanoparticle and its plasmonic response.

2. Introduction

In the last 30 years, many efforts in research and development have been devoted to understanding the relation of the atomic structure of nanomaterials and their physical and chemical properties. For that, many characterization and analytic techniques have been developed to achieve atomic resolution and to register information, and many synthetic and tuning methods have been designed to modify these properties, both at the nanoscale. Furthermore, the different electronic distribution of different nanostructured materials leads to various electronic events to occur when electromagnetic fields interacts with them, opening a wide range of possibilities in nanotechnological applications.

Noble metallic nanoparticles (NPs) have captured the attention of the scientific community in the last decades due to their interesting optical properties [1, 2]. Their origin comes from the localized surface plasmon resonances (LSPRs) response because of coherent electronic oscillations of the conduction and valence electrons. This optical response can be tuned by modifying the composition, size, shape, and dielectric environment of the NPs [3, 4]. Furthermore, the plasmonic response varies with the application of electromagnetic external fields since it is an electronic phenomenon. The direct consequence of the interesting optical properties easy tunable that plasmonic NPs present is their promising application in photonics and optoelectronics [5, 6, 7]. Indeed, they are widely employed in sensing, photodetectors, surface enhanced Raman spectroscopy (SERS), drug delivery, cancer therapy…

Different noble metallic NPs have been widely studied in this area of research, including single metal NPs, bimetallic NPs and metal-organic systems including Au, Ag and Pt [8, 9]. However, Au-NPs are of great interest for three main reasons. The first one is the well-known facile shape, size, and surface functionalization control inherent to the synthetic approach. Gold nanorods, nanorings, hollow NPs, nanodumbbells, and nanostars among others have been reported [1, 4, 10, 11]. The second reason is that they present enhanced light-related events like absorption, scattering and SPR. In addition, Au-NPs support SPR in the wide UV-vis-near-IR electromagnetic spectrum range [12, 13]. The third one is related with the medical application field of Au-based systems, which provides a lot of information about synthesis, functionalization, and optical response of these kind of particles, including cancer imaging, photothermal therapy, and single-molecule detection, sensor fields, to add to the applications mentioned above [14, 15, 16].

The study of the plasmonic response in NPs is not trivial. Many options related with light absorption in UV-vis to near IR spectrophotometers have been widely used to get information about the NPs from their interaction with light. However, this information is not related with

the LSPR but with the optical response of plasmonic NPs suspension. One of the best ways by far to observe single NPs and localize their surface plasmons at high spatial resolution is to use scanning transmission electron microscopy (STEM) combined with electron energy loss spectroscopy (EELS) studies [17, 18]. In this work, the existing literature concerning STEM-EELS local experimental studies and theoretical simulations on plasmonic Au-NPs optical response is briefly reviewed. Furthermore, EELS raw data about Au-NPs of different sizes and shapes obtained by using a probe-corrected and monochromated STEM are treated to extract plasmonic information.

3. Surface plasmons

The main objective of this section is to understand the physics and phenomena behind the surface plasmon (SP) features. From an historical point of view, it is interesting to known that more than 2000 years ago, the Romans took profit from this optical phenomenon. Indeed, they used noble metallic NPs in staining of glass for obtaining a product much more visually appealing by a set of bright metallic colors never achieved before. Since this effect can be explained by the classic physics without considering quantum mechanics, only applicable in sub-nanometric objects, taking into account electromagnetic fields and their interaction within the metallic NPs. The basic foundations were stablished and developed by Mie in 1908 [19].

Surface plasmons are based in the collective electronic excitations of conduction metallic band electrons. Their origin resides in the capacity of SP to capture, concentrate, and propagate electromagnetic energy as an evanescent wave when they are exposed to an electromagnetic excitation. Therefore, it is interesting to describe theoretically what evanescent waves implies. Considering an electromagnetic wave in two dimensions localized in a medium with refractive index, *n*, it can be described by the electric field, *E*, associated with it (Equation 1).

$$E = E_0 \cdot e^{j \cdot \omega \cdot t - j \cdot \mathbf{k} \cdot \mathbf{r}} \qquad \textbf{(1)}$$

Where E_0 is the electric field amplitude, t is time, j is the imaginary number $(-1)^{0,5}$, ω is the wave frequency, and $\boldsymbol{k}$ and $\boldsymbol{r}$ are the wave and position vectors, respectively. Therefore, the product $\boldsymbol{k} \cdot \boldsymbol{r}$ represents the wave function at each spatial coordinate (x, y, z). Note that when the exponent of this function is complex, the wave is propagating in that medium; if it is not, it is a stationary wave. SPs can be either propagating waves or stationary ones leading to the so-called surface plasmon polaritons (SPPs) and local surface plasmons (LSPs), respectively. Both situations are developed in sections below in detail.

Considering a propagating wave with the vector ***k*** parallel to the propagation direction, its module, *k*, is the root square of the three orthogonal components summation, and it can be expressed like in Equation 2, as a function of the wavelength, λ, and the propagation velocity in the vacuum, *c*, as the newly introduced parameters. At this point, it is interesting to study the propagation of the wave through an interphase dividing two media of different refractive index, n_1 and n_2. For simplify the calculations, one of the orthogonal components of the wave can be zero by choosing the direction or angle of incidence of the light beam. Then, the problem must comply the two-directional expression given by the Snell's law considering the incident angle, α, and the refracted one, β, as presented in Equation 3.

$$k = n \cdot \frac{2 \cdot \pi}{\lambda} = n \cdot \frac{\omega}{c} \qquad \textbf{(2)}$$

$$n_1 \sin \alpha = n_2 \sin \beta \qquad \textbf{(3)}$$

In addition, note that the two Cartesian components x (parallel to the interphase) and y (perpendicular to the interphase) are different from zero. However, the direct conclusion that can be extracted from Snell's law is that the component parallel to the interphase do not change during refraction, while component y decays exponentially, resulting in an unique propagating wave parallel to the interphase that can be expressed again as an electrical evanescent field, E_2, as shown in Equation 4.

$$E_2 = E_0 \cdot e^{-k_{y2} \cdot y} \cdot e^{j \cdot \omega \cdot t - j \cdot k_x \cdot x} \qquad \textbf{(4)}$$

It is important to note that only by changing the dielectric properties, this is the refractive index, at the proximities of the interphase (where the y component is not negligible), there is a modification of the electromagnetic field. Summarizing, the evanescent field presents high sensibility in the interphase region leading to significant changes in the SP response by changing dielectric properties of the medium [20].

3.1. Plasma model: the dielectric function

The plasma model describes the optical properties of metals by doing several considerations to simplify calculations, which are out of the scope of this work. The interesting point is that they can be explained by considering the metal as a gas of free electrons moving in the surroundings of stable background of cations cores. For noble metals, the frequency range at which this model is applicable excludes UV region because at small wavelengths the contribution of the free electrons does not dominate the bound-electron contribution; that is the reason why the plasma model for noble metals at the mentioned frequency range is known as Drude model as well

[21]. The resulting dielectric function of the free electron gas $\varepsilon(\omega)$ extracted from these models is presented in Equation 5.

$$\varepsilon(\omega) = 1 - \frac{\omega_p^2}{\omega^2 + j \cdot \gamma \cdot \omega} \qquad \textbf{(5)}$$

Where ω_p is the plasma frequency that depends on the electronic characteristics and γ is the collision frequency (relaxation time of the free electron gas reciprocal). Last expression is composed by a real and an imaginary component. When $\omega < \omega_p$, the metallic character is important so the imaginary component is increased due to the interband transitions effect at this frequency range, resulting in a good fit of the experimental data with the model explained, as shown in *Figure 1* for gold as a characteristic noble metal. However, the Drude model for this metal is not applicable from the visible region because of the interband transition effect.

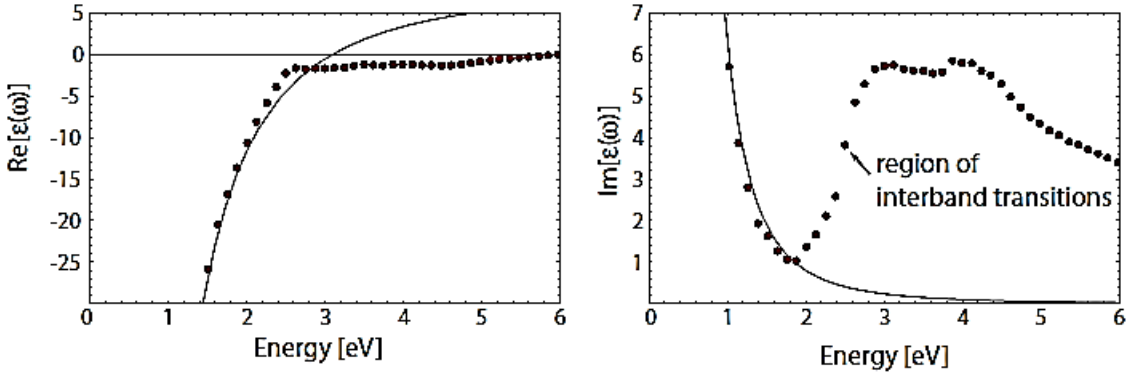

Figure 1. *Theoretical gold dielectric function of the free electron gas (solid line) fitted to experimental data (dots) for real (left) and imaginary (right) components. Experimental data have been obtained from Johnson and Christy, 1972. Extracted from reference* [22].

Finally, it can be considered that $\omega > \omega_p$ where, the propagation of transversal electromagnetic waves is not forbidden as in the case studied previously. The consequence of that is the longitudinal collective oscillations of electrons in the conduction metallic band opposed to the cations background used in plasma model. This kind of excitation is called volume plasmon. This is important because it is the only case in which not only conduction, but valence electrons can be excited in dielectrics to observe a plasmonic response. Once the fundamentals of propagating wave and related excitations have been described in a general view, in sections below the stationary, non-propagating waves plasmonic responses are developed.

3.2. Localized surface plasmon resonance

Localized surface plasmons (LSP) are stationary excitations of conduction metallic bands when they are coupled to an oscillating electromagnetic field originated by exposing the NP to direct light. Typically, these modes are related to scattering problems of objects which dimensions are smaller than the wavelength of the light source and appears naturally on curved surfaces that exceeds the effective restoring force on excited electrons to produce a resonance effect amplifying the plasmonic response in both, the surface and the near-field regions in the NP's surroundings. Therefore, LSP are known as well as LSPR, as introduced before. It must be outlined that there is not only a propagation difference with SPP, but the foundation of the oscillation itself in relation with (a) NP size and shape, (b) light wavelength and (c) localization of the response must be considered to characterize the optical properties of the material.

In Au and Ag NPs, the LSPR is in the visible region of the electromagnetic spectrum, leading to transmit (light absorption events) and reflect (light scattering events) light showing bright, resonantly enhanced colours, giving an explanation to the classical ornamental uses of noble metals NPs. For understanding the LSPR response of materials considering the features mentioned previously, a model for the classic spherical particle of diameter $d << \lambda$ is developed theoretically, and presented below, using the quasi-static approximation applicable to NPs smaller than 100 nm, but big enough not to be affected by quantum mechanics (i.e. above 10 nm) [22]. For NPs bigger than 100 nm, a more complete electrodynamic theory is needed to explain scattering and absorption events; this is the Mie theory.

3.2.1. Quasi-static approximation for a spherical NP

Considering a regular spherical metallic cluster with radius a in an applied uniform, isotropic electrical field E_0 and its dielectric function as a complex number ε [1] in a non-absorbing environment with dielectric function ε_m. The electric field inside the nanosphere (E_{in}) and the electric polarizability (α) due to the external field can be expressed as shown in Equations 6 and 7, respectively. Taking profit from the curved boundary between absorbing and non-absorbing media and the polarization (p) understood as a dipole moment in the sphere defined as $p = \varepsilon_0 \varepsilon_m \alpha E_0$; where ε_0 is the vacuum permittivity. The E_{in} and α are:

$$E_{in} = E_0 \cdot \frac{3\varepsilon_m}{\varepsilon + 2\varepsilon_m} \qquad \textbf{(6)}$$

$$\alpha = 4\pi\varepsilon_0 a^3 \cdot \frac{\varepsilon - \varepsilon_m}{\varepsilon + 2\varepsilon_m} \qquad \textbf{(7)}$$

[1] To make calculations and equations simpler, the dependence of the dielectric function with ω is not considered in this section, and it is just treated as a complex number ε.

The resonantly enhanced plasmonic response comes from the case in which the denominator of both, E_{in} and α, is minimum since they achieve their maximum value. When the imaginary part of the dielectric function is not relevant, the resonant response is called the dipole surface plasmon, complying the Fröhlich relation showed in Equation 8. Furthermore, in relation with the Drude model (see Equation 5), this resonant frequency ω_r corresponds to the expression in Equation 9, demonstrating the dependence of this resonantly enhanced plasmonic response with the dielectric environment [22, 23].

$$\varepsilon(\omega) = -2\varepsilon_m \quad \textbf{(8)} \qquad \omega_r = \frac{\omega_p}{\sqrt{3}} \quad \textbf{(9)}$$

However, only the electrical response inside the NP have been considered in the explanations above, but there is an electrical response as well at distances near the spherical surface. Even the convenient equations are not showed in here, the resonance response are related with the last ones since the denominator of the corresponding expressions is $\varepsilon + 2\varepsilon_m$.

3.2.2. Mie theory

Last approximation is limited to NPs typically smaller than 100 nm, as commented before. In the cases in which the NP induce a phase-change in the driving field, an electrodynamic study is needed. This is the theory developed and published by Mie in 1908 fathoming in the physical scattering and absorption events in a sphere, trying to understand the colours of a NPs colloidal solution [19].

First consideration of this theory is that it was realized by using classic electrodynamic terms, so any relative modern concept as plasmon or electronic motion and related events are considered from a physical point of view. Mie theory has its origin in applying the Maxwell's equations using multipoles expansions concerning the electromagnetic fields acting on a metallic NP with a spherical fixed shape, and (a) particle size, (b) optical function of the NP and (c) optical function of the environment. For that, two sets of scalar electromagnetic potentials (electric & magnetic functions) were determined to extract different fields of interest.

These sets of potential have been substituted by other notations such us the one proposed by Stratton by doing a more formal mathematical description of them. These are the vectors $\boldsymbol{M}$, $\boldsymbol{N}$ and $\boldsymbol{L}$, corresponding to magnetic, electric and a term composed by the differential operation of the scalar function, respectively. The interesting point in here is that the order of the partial waves, L, extracted from the latter vector, represents the order of spherical multipole excitation in the metallic NP since it corresponds to the spherical harmonic functions of $\boldsymbol{M}$ and $\boldsymbol{N}$. In other words, L = 0, 1, 2 and 3 means longitudinal, dipole, quadrupole and octupole modes excitation.

However, to locate spatially these modes, the quasi-static approximation limit must be considered applying the Mie theory, since Equations 8 and 9 do not explain reality of noble metals in which the imaginary part of the wave function is much more relevant than in alkali metals even in the proximity of the resonance. This is done by modifying the expression for the term α considering the resonance energy shift due to the retardation of the exciting and depolarization fields, with its origin in the NPs volume. In spectroscopic terms, this means that in Drude model only intraband transitions (sp-sp) were explained, while interband transitions (d-sp) are introduced in the latter model. Furthermore, another change in the α is introduced by the model defining the radiation damping as a decay path of coherent electron oscillation into photons, with the weakening of the dipole plasmon resonance strength for more voluminous NPs as the main consequence. The formal meaning is that the resonant modes $\omega_{r,L}$ can be defined and localized, as shown in *Figure 2*, by the Equation 10.

$$\omega_{r,L} = \frac{\omega_p}{\sqrt{1 + \frac{L+1}{L} \cdot \varepsilon_m}} \qquad \textbf{(10)}$$

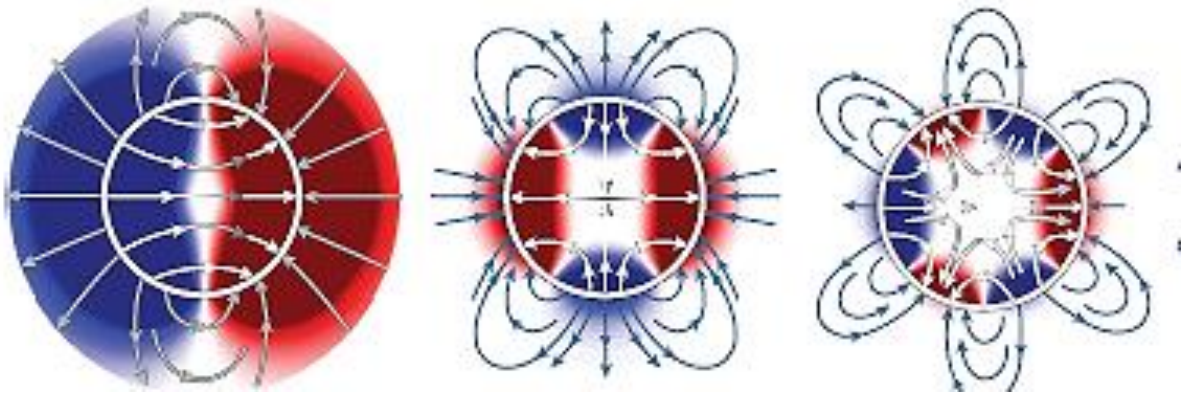

Figure 2*. LSP electric potential with its positive (red) and negative (blue) component in spherical dipole (L = 1), quadrupole (L = 2) and octupole (L = 3). Electric field lines corresponding to a punctual electric charge located in the x-axis outside of the sphere are represented as well. Extracted from reference* [24].

4. Transmission electron microscopy

First transmission electron microscope was developed by E. Ruska and M. Knoll in 1931 for improving the capabilities of the optical microscopes. Ruska was awarded by the scientific community with the Nobel prize in physics in 1986 [25]. The foundation of TEM is the transmission of an electron beam through a thin sample previously focused by an electron optical system to finally enlarge the object into an image on a fluorescent screen, see Figure 3.

The electrons are extracted from a sharp refractory metal tip by thermionic or field emission and accelerated up to voltages between 60-300 kV, typically. The electron beam is condensed by a set of condenser electromagnetic lenses to pass through an aperture before illuminating the sample. The transmitted electrons with the diffracted ones are redirected by another set of objective electromagnetic lenses and used to get the diffraction pattern or the projected image of the sample on a phosphorescent screen or a charge-coupled device (CCD) camera or even more recently to direct electron detectors. TEM is a robust microscopic technique that can get spatial resolutions down to few tens of picometers depending mainly on the electron source wavelength, the lenses design and the aberration correcting system. Furthermore, the possibility to add some detectors to analyse different kind transmitted and scattered electrons makes possible to realize the previously mentioned spectroscopic analysis.

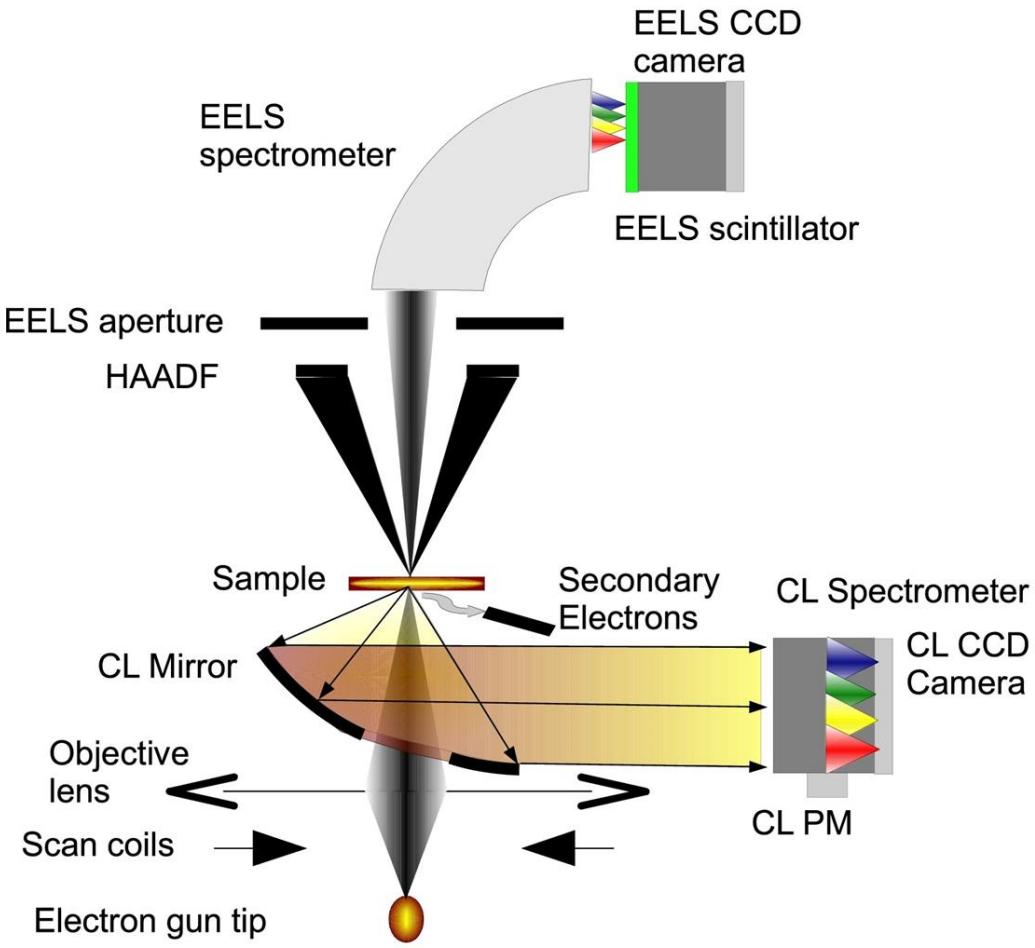

Figure 3. *Scheme of the components and design of STEM mode. Extracted from reference* [26].

The resolution, *r*, is defined as the smallest distance between two points or lines that can be resolved by an electronic microscope. Using the Rayleigh criterion for visible-light microscopy, it is restricted to the wavelength of the radiation, λ, the refractive index of the viewing medium, μ, and the semi-angle of collection of the magnifying lens, β, as $r = 0.61 \cdot \lambda / \mu \cdot \sin \beta$.

Furthermore, it is a relation between the energy of the electrons and their wavelength defined by de Broglie's relation; and these two parameters are related as well with the accelerating voltage of the electron beam in a TEM. This is, by using an accelerating voltage of 100 kV, and being $\mu \cdot \sin\beta = 10\, mrad$ the numeric aperture, which are typical values of operation, a resolution of 0.22 nm is achieved [27].

Otherwise, STEM is the best TEM-based technique to get images and analytical information point-by-point with sub-nanometric resolution by using a highly focused convergent probe from a bright electron source to avoid spatial incoherence. Depending on the electrons collected by the detectors, or more precisely the values of the scattering angles of such electrons, different detectors (and then techniques) can be used (developed), i.e. bright-field STEM (BF-STEM), annular dark-field STEM (ADF-STEM) and high-angle annular dark-field STEM (HAADF-STEM), by collecting the direct transmitted electrons with a circular detector, the diffracted ones with an annular detector and the thermal diffuse scattered ones at high angles with an annular one, respectively, as shown in *Figure 3*. In this work, STEM studies were realized by using FEI Titan Low-Base microscope equipped with a Cs probe corrector, a monochromator and an ultrahigh X-FEG electron gun, working at an acceleration voltage of 80 kV.

The interaction between electrons and the specimen analysis can be used as well for obtaining spectroscopic information such us EELS by employing an EELS-spectrometer. Regarding plasmonic NPs, STEM-EELS is one of the best combined techniques for characterizing optical responses at the nanoscale [17, 18].

4.1. Electron energy loss spectroscopy (EELS)

EELS consists in the analysis of the kinetic energy loss of electrons when they are transmitted through a TEM sample by using a detector working as a spectrometer. This information can be related with the chemical composition and with the electronic distribution of the material; thus, information about the electronic and optical properties of the materials can be obtained with an energetic resolution down meV [26, 28]. Most of the primary electrons that reach the sample pass through it without losing energy, resulting in an intense peak in the spectrum at the zero point called the zero-loss peak (ZLP). However, the most interesting spectrum part comes after the ZLP: the low-loss region below 50 eV energy loss, corresponding to the inelastic scattering with volume and surface plasmons (and inter/intraband transitions) in the specimen, and the core-loss region above 50 eV, which is mainly related with the composition and atomic configuration of the analysed material. For obvious reasons, the low-loss region of the EELS spectrum is discussed in detail below.

4.1.1. Low-loss EELS

Regarding plasmonic modes defined in previous sections, EELS have been widely used to determinate the plasma frequency of metals [30]. Historically, the first identified low-loss region was in the pioneering experiment realized by Ruthermann in 1941 using Al thin films [31]. The peaks observed were then defined as bulk plasmon by Bohm and Pimes in 1952 [32]. In the same way, LSP modes were first described theoretically in 1968 by Fujimoto and Komaki, and Crowell and Richie, simultaneously [33, 34]. They predicted the existence of two different modes called bright and dark modes, corresponding to the presence of a dipole moment in a set of NPs or not, respectively. Bright mode was confirmed experimentally by Kokkinakis and Alexopoulos in 1972, while the report of the dark modes by Wang and Cowley needed to wait for the advances in TEM with the STEM and its combination with EELS in 1987 [35, 36].

The pioneering work realized by Nelayah et al. in 2007 was the first published in which LSP modes were identified by mapping the energy loss in the low loss region of the EELS spectrum. In that case, the sample was Ag triangle-shaped NP, being able to map three main modes with ω_A = 1,75 eV, ω_B = 2,70 eV corresponding to surface plasmons and ω_C = 3,20 eV corresponding to the bulk plasmon resonance for silver, as presented in *Figure* 4a [17]. However, other important studies have been realized to explore not only the influence of the shape but of the composition as well in last decades for mapping other modes, as commented before. In the paper published by Arenal et al., Au and Au-Ag bipyramidal-shaped NPs were studied by STEM-EELS. For the former one, four modes were found in the low loss region at ω_A = 1,1 eV, ω_B = 1,55 eV, ω_D = 1,85 eV, corresponding to LSPR modes, and ω_C = 2,45 eV due to the composition [3], as presented in *Figure 4b*. The study realized by Nicoletti et al in 2013 showed the three-dimensional optical response, LSPR components of a silver nanocube by combining electron tomography and EELS studies [37], as shown in *Figure 4c*.

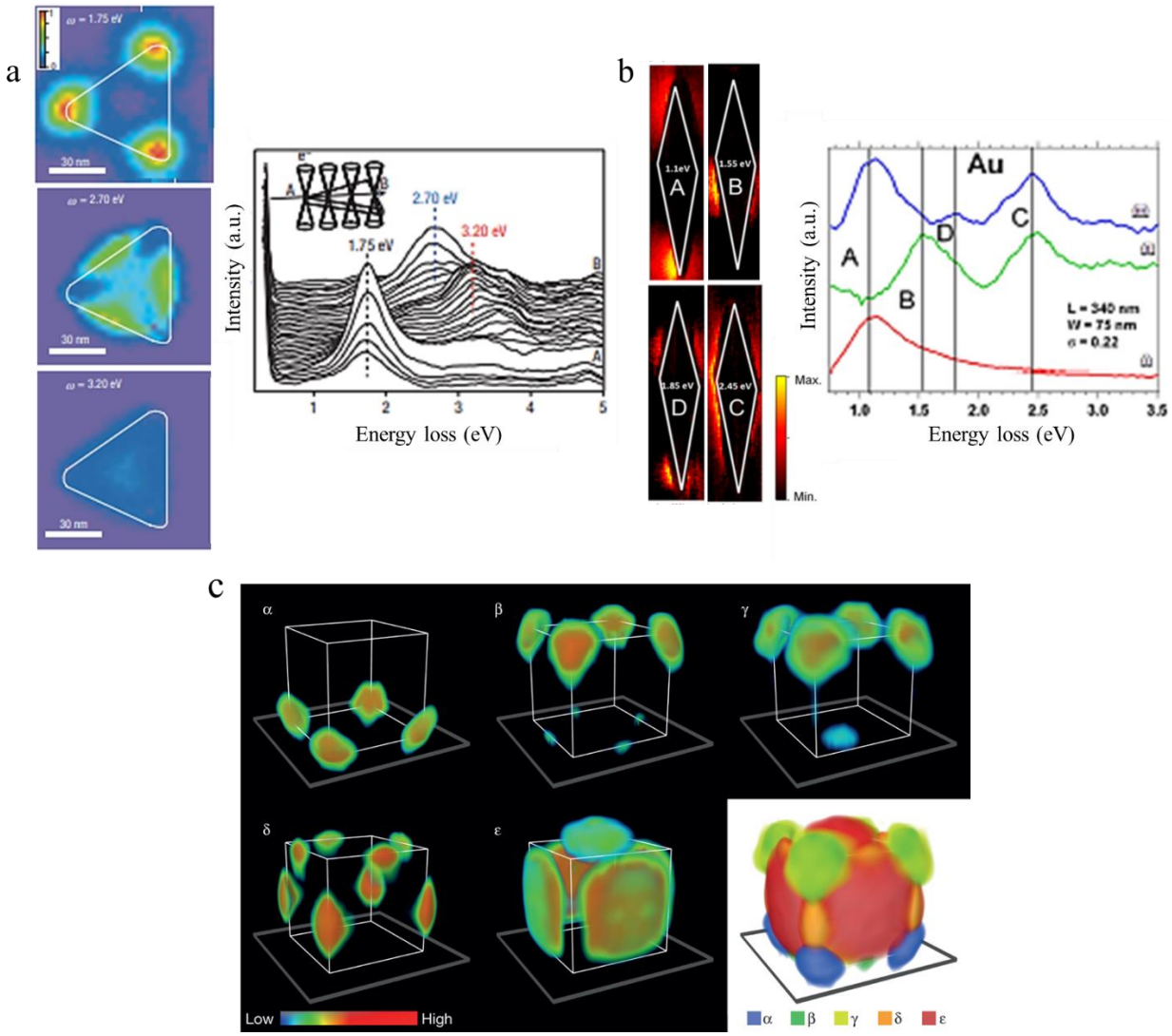

Figure 4*. Low loss EEL spectrum of (a) Ag triangle-shaped NP, (b) Au bipyramidal-shaped with the map of their corresponding modes, and (c) 3D visualization of the LSPR components of a silver nanocube by combining tomography and EEELS data, from references* [17], [3] and [37] *respectively.*

It is worth mentioning that this kind of analyses require, at least for complicated cases, the combination of these EELS measurements and computational simulations. Several theoretical approaches have been developed for solving Maxwell equations once the plasmonic nanostructures are already known (size, morphology, composition and dielectric environment are defined). These computational methods can be classified into frequency dependent ones, as discrete dipole approximation (DDA) or boundary element method (BEM), and time-domain methods, which are less used than the former ones for EELS studies [5, 24, 29].

5. Methods

The gold nanoparticles used in these works were prepared based on the seed-mediated technique using silver nanocubes as seeds. In this case, these silver nanocubes with 50-70 nm mean sizes were added into the reaction mixture of two different capping agents, CTAB and F-127, to finally obtain star shaped branched gold nanoparticles. The concentration and quantities of CTAB and F-127 have been controlled for modifying the shape and size of the NPs. The produced nanoparticles were then stirred for at least 30 min. The powder was recovered by centrifugation, washed several times with water to remove the solvent and any other unreacted starting materials, and finally suspended in DI water to avoid any particle agglomeration.

TEM-EELS data was recorded using a probe-corrected FEI Titan Low-Base 60-300 kV STEM equipment, operated at 80 kV and equipped with a Cs probe corrector, a high-brightness X-FEG gun, a monochomator and a Gatan Tridiem 866 ERS energy filter. Fifteen EEL spectra (of 10 ms/each) were acquired for each probe position following a two-dimensional (2D) region across the nano-object. The convergence and collection angle were 25 and 35 mrad, respectively. Typical energy resolutions (full width at half-maximum of the ZLP) of the measurements were better than 180 meV. EEL spectra were acquired using the spectrum-imaging (SPIM) mode [38, 39]. For the data analysis, each EEL spectra were aligned along the ZLP and its tail was removed using a power law subtraction method [28, 40]. Furthermore, energy dispersive X-rays spectroscopy (EDS) has been carried out in parallel for analysing the chemical composition of these nanostructures using the same acquisition conditions.

Regarding the data analysis, two main issues must be considered to be able to interpret accurately the data: the background removal and the different contributions of the plasmonic features. As mentioned before, the signal of the elastically transmitted electrons, ZLP, is very intense in comparison with the rest of the signals and then, at some point it renders difficult the analysis. In the low-loss region, this aspect is even worst. Typically, the removal of the ZLP is made by using a power-law function to fit it. In this case, it can be used for qualitative analysis since some signals of the low-loss region can be extracted from that treatment but above ~2 eV. Regarding the plasmonic features, even if we got the background removed, some plasmonic modes below last value may be shadowed or even different plasmonic modes can be overlapped so the energy resolution that the system has is not good enough to distinguish both. To solve these problems, hyperspectral analysis, and multivariate analysis (MVA) have been widely used. The idea of using these methods is to represent each SPIM dataset's component as a product of two different matrices: one containing the spatial information, and the other containing the spectral information; leading to a linear mixing model.

Principal component analysis (PCA), developed by Pearson in 1901 [41], offers a solution for the last approximation. This method has been applied to EELS analysis by Trebbia in 1990 [42], and since these seminal works, it has been widely used for EELS and related analysis. The basic imposition of this analysis is the orthogonality between the different spectral components with the main aim of minimize the distance between the solution and the experimental data. For that, it is crucial that the variance of the signal is higher than the noise variance of the spectrum. However, the imposed orthogonality means that some regions of the EELS spectra will be negative even though it is not real, and it has any physical sense. Summarizing, PCA is a powerful hyperspectral analytic tool used to decompose signals (given a number of components and a variance threshold) after denoising the data, cheap computational method, but other method should be used to avoid hard interpretation efforts specially in the low-loss region [43]. Without going into detail, here is where blind source separation methods play an important role since it is possible to get positive values in the whole range of the EELS spectra using them. The most used variation of PCA for this kind of studies is the non-negative matrix factorization (NMF), consisting in the decomposition of each data into the linear combination of the basis vectors. One of the main limitations of NMF is that, to achieve a good approximation, the intrinsic properties of the system must be visible in a wide enough range.

In this work, a data analysis solution for the main drawbacks above mentioned has been used. This approach has been developed under the framework of the PhD thesis of M. Peláez-Fernández at the LMA-INMA-U. Zaragoza [44]. This method consists in the subtraction of the ZLP not fitting the signal but treating the most intense peak as a component itself, choosing the signal of a region in where it is any plasmonic response neither noise, and then extracting the background from the other SPIM components. To optimize the analysis time and the computer performance, not all the energy channels of the SPIM have been used, but only from to 0.2 eV to 3.5- 4.0 eV (depending on the sample) since it is the region of interest. Once the background has been extracted, this method applies the NMF algorithms. It performs the component decomposition with an arbitrary component number introduced (from 10 to 16 in the samples studied in this work), and it gives back the individual data for each component. It is important to outline here that not all the numbers of components are proper for every energy range, so different attempts have been launched for every single sample to get the real components independently from the others. In addition, following the same line, different energy windows have been tested to get the proper modes in order to avoid important noise contributions.

6. Results and discussion

The plasmonic response of four different gold nanostructures have been studied: (1) spheroidal anisotropically branched nanoparticles, (2) multipods branched irregular nanostructures, (3) arrowhead nanobjects and (4) dendritic structures. All these nanomaterials have been produced under the framework of the PhD thesis of M.C. Ortega-Liebana at the INA-U. Zaragoza, see above [45]. Thus, different STEM-EELS studies of Au-based different-shaped NPs obtained from the last samples are presented below, and the results are discussed.

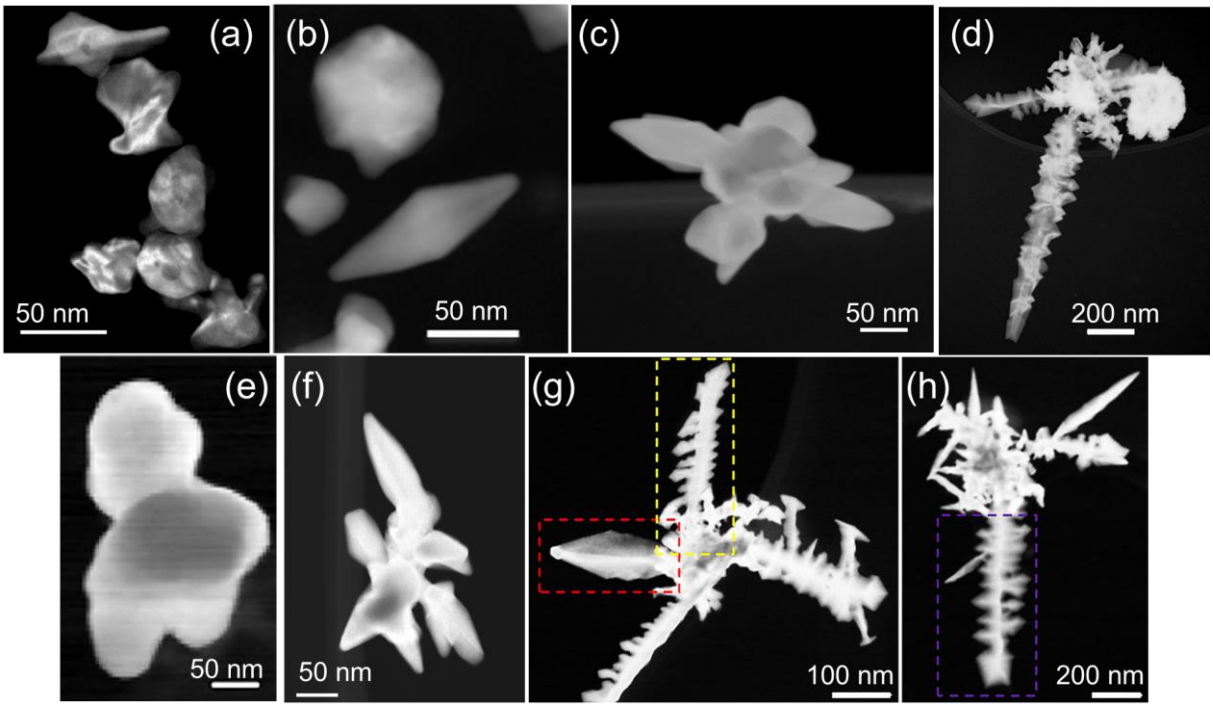

Figure 5*. HAADF-STEM micrographs for (a to d) different samples synthetized by M. C. Ortega-Liebana, and for the nanostructures studied in this work, being (e) spheroidal anisotropically branched, (f) multipods branched irregular, (g- red dashed-line rectangle) arrowhead and ((g -yellow dashed-line rectangle), and (h, purple dashed-line rectangle)) dendritic nanoobjects, respectively.*

Regarding the chemical compositional analysis, *Figure 6* shows the selection of some of these EDS data. As we can see, some silver, in low quantities and localized, can be found on them because of the silver seed used for the synthesis. This silver will contribute in the plasmonic response of such nano-objects as it will be discussed later.

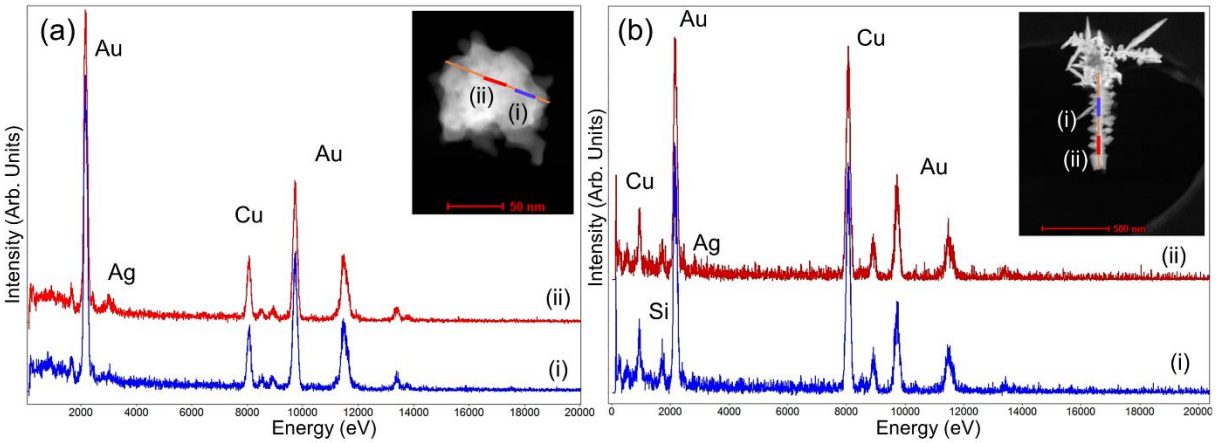

Figure 6*. Selected EDS spectrum-line of (a) a spheroidal NP and (b) a dendritic NP, with their corresponding HAADF images. In both cases, the spectra have been registered following the orange line path, being (i) and (ii) the summation of 8 spectra at different regions of the NPs.*

Note that the silver content is much lower than the gold's one in both NPs, and it is highly localized. This is because of the small cubic seed used to build the nanostructure and the large amount of gold used in comparison with the first. However, the other interesting information that can be extract is that the silver content is appreciable in *Figure 6a*, probably because of the lack of pods or dendritic-type structures emerging from the silver core, while it is not appreciable at all in *Figure 6b*. Summing up, it can be expected that the certain appreciable amount of silver in spheroidal nanostructures may contribute to the plasmonic response of the NP, while for more complex shapes and bigger sizes it could be any contribution.

6.1. Spheroidal anisotropically branched nanoparticles

Figure 7 corresponds to the analyses of these spheroidal anisotropically branched nanoparticles, see HAADF-STEM image. Maps of the different LSPR modes of these nanostructures and their corresponding EEL spectra can be observed in this figure. These objects present an irregular shape but with spherical boundaries which will determine the great part of the responses. Moreover, it is expected to observe a characteristic signal of gold since it is its main component above 2.0 eV (see *Figure 1*) [3, 4, 13], or even of silver at higher energy losses [3, 18].

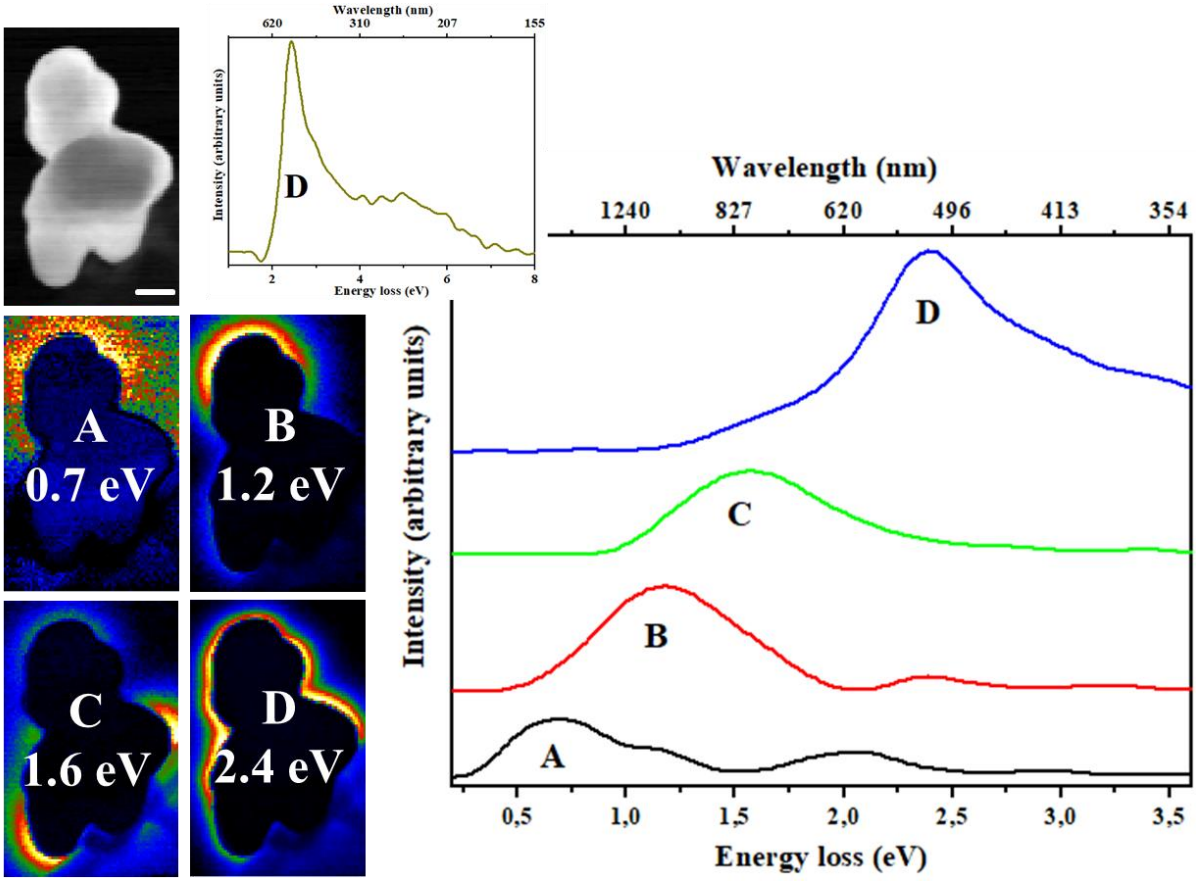

Figure 7*. Plasmonic features of spheroidal anisotropically branch NP. (a) HAADF-STEM micrograph with a scale bar of 50 nm and the abundance maps of the components at the specified low-loss region energy (A to D). (b) Spectra of the different responses obtained. (c) EELS spectrum of the 2-8 eV range obtained by subtracting the background of the original SPIM.*

The wideness of the peaks indicates that several LSPR modes are contributing to that signals in each of these energy regions. In addition, even though the procedure have been followed to differentiate independently every single mode, it can be seen the contribution of other modes at the same region, as in the 0.7 eV mode, where two other signals can be observed at 1.1 eV and 2.1 eV. The wide peak appearing at 2.1 eV probably corresponds to the surface mode of gold, but it has not been possible to isolate it for its detailed analysis. As mentioned before, this NPs can be roughly interpreted like an arrangement of spherical NPs, so many of the modes localized in this study can be referenced with that basis. The lower energy mode A at 0.7 eV has not been reported probably to the low energy at which it appears that means that the contribution of the ZLP may totally shadow this signal. However, it is localized at the upper spherical borderline of the NPs and spread further from the NPs surface, where the mode B at 1.2 eV is most localized. This is likely due to the lower signal-to-noise ratio of this response. Indeed, the difference in the noise of these two signals is attributable to the relative intensity of their peaks, so it is difficult to extract information from the less intense peak at that region. B response

appearing at 1.2 eV is, as in the last mode, another longitudinal mode. As commented before, these modes are hardly related with the size and shape of the NP under study. In other works, similar modes have been reported for Au-based regular nanostructures and they were able to assign them to a longitudinal, L = n value according to the Drude model, as in reference [46]. In this case, it is not that easy because of the irregular spheroidal shaped-NP. The same conclusion can be extracted for mode C at 1.6 eV which is longitudinal as well but localized on another spheroidal region of the NP. The mode at 2.4 eV is the transverse mode since it has been reported at this energy [47, 13]. Note that this signal does not decay to zero after the maximum. This is because there is an intense, wide peak localized around 5.0 eV due to the carbon where the sample is deposited on, as shown in Figure 5c. This contribution has already been reported [3, 10]. In addition, looking carefully at the D spectrum, a slight signal can be identified at 3,0 eV but it has been unavailable to isolate this peak due to the intensity of these last two signals at both sides. The latter one may correspond to a transversal mode of silver [3, 8, 17].

6.2. Arrowhead nanobjects

In *Figure 8*, the obtained low-loss region components spectra are presented together with their corresponding abundance maps for these arrowhead nano-objects. These structures can be seen as prismatic bipyramids, excluding the signal coming from the dendritic nanostructure (see *Figure 5*). Thus, our present analyses can be compared and based on previous studies on bipyramidal-shaped Au-nanostructures [3].

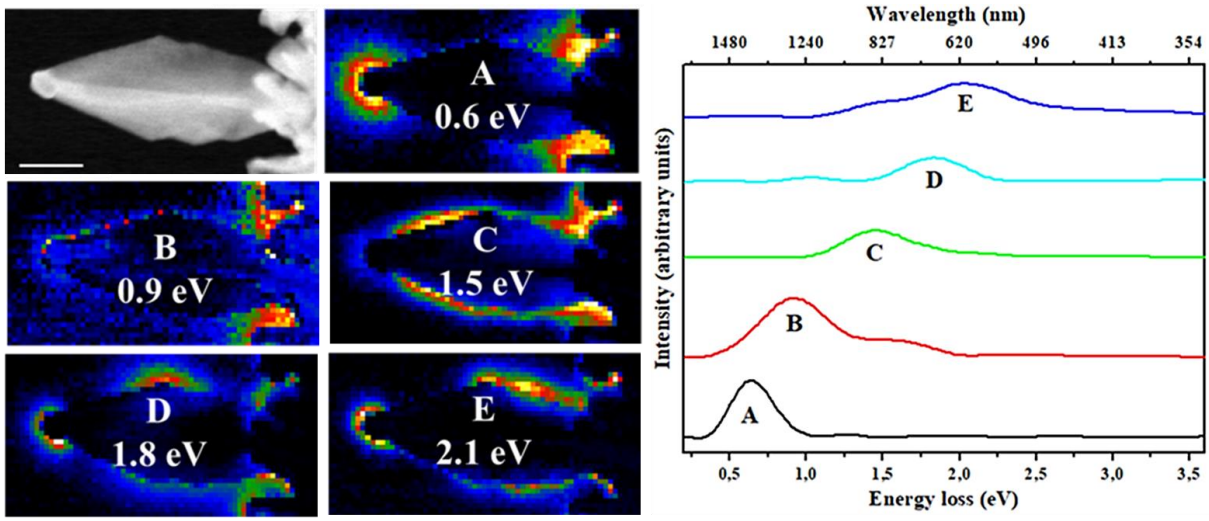

***Figure 8**. Plasmonic features of arrowhead Au-nanostructure. (a) HAADF-STEM micrograph with a scale bar of 50 nm and the abundance maps of the components at the specified low-loss region energy (A to E). (b) Spectra of the different responses obtained.*

These identified LSPR modes appear at 0.6, 0.9, 1.5, 1.8 and 2.1 eV for A, B, C, D and E, respectively. The two at lower energies are the most intense and sharp because while with increasing the energy in the low loss region the peaks turn into less intense and broader ones because of two main related reasons: the higher cross-section at those frequency values and the highly localized field intensity at the sharpest tips [3]. As in previously studied cases, not all modes have been identified independently from the other so small contributions appears in different spectra. The most notable cases are the contribution of C and D-modes to B plot and the C-mode contribution to the most energetic E mode.

The A mode has not been reported at this energy before probably because the ZLP tail shadow signals lower than approximately 1,0 eV for the high contribution of the transmitted electrons without losing energy. However, it is the same dipolar mode appearing in bipyramidal-shaped NP at 1.0 eV, but displaced due to the slightly spherical tip. The B-mode at 0.9 eV is mainly localized at the tip of the bipyramid, as in the latest case, so it is a long apex focalized mode, despite the most intense regions are not in the aim nanoobject but in the right part, being part of the whole NP presented in *Figure 8a*. The C-mode at 1.5 eV, as it can be observed, has a contribution on both, the short and the long apex. There is also a contribution at this energy for other objects that are close to the structure of interest. Finally, the D-mode at 1.8 eV is mainly localized on the short apex, but there is a contribution of the B-mode leading to an intense region at the tip of the nanoobject. The A-B, C and D-modes are typical for bipyramidal-shaped NP, and their intensity and position are related only with the size and shape since they are longitudinal modes. They correspond to dipolar (L = 1), quadrupolar (L = 2) and octupolar (L = 3) modes, respectively, according to reference [3]. Furthermore, the latter one appears only for large enough NPs. The last E-mode can be assigned to a transverse dipolar mode mixed with another quadrupolar one [3]. There is a small shift of this mode that can be due to some size or changes of dielectric environmental changes [3, 4].

6.3. Multipods branched irregular nanostructures

Figure 9 concerns the study this other kind of nanostructures. In this case, the shape of the NP is much more irregular than in the previous ones because of the different sized, shaped pods grown from the silver core. These complex nanoparticles render very difficult the interpretation of the modes as it is difficult to run simulations for reproducing such responses.

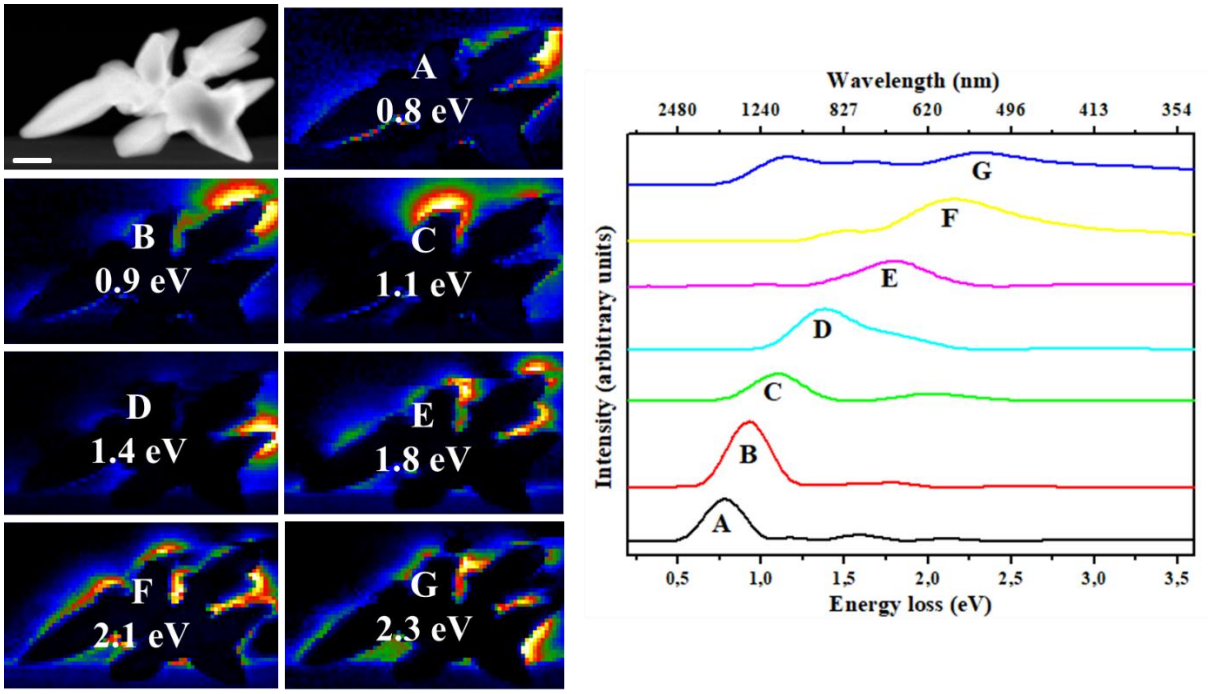

***Figure 9**. Plasmonic features of multipod branched irregular Au-nanostructure. (a) HAADF-STEM micrograph with a scale bar of 50 nm and the abundance maps of the components at the specified low-loss region energy (A to G). (b) Spectra of the different responses obtained.*

As it can be seen, seven different modes have been identified. The two more intense and better-defined modes have been the first ones, A and B, coinciding with the previous analyses. However, the signal for C has been multiplied by 150 arbitrary units in intensity for a clearer representation in the spectrum (*Figure 9b*). A possible question could be is this mode is real or notable enough to be presented in the results even its low intensity. Looking at the abundance map obtained from this mode, it seems that it is highly localized at that point and the contribution of that signal can be observed in the spectrum G, so it has been considered as a real one. Again, as the modes appears at higher energies, the contribution of the less energetic but intense peaks is appreciable as in latest case, as explained in last example.

The modes A to D are highly localized at the sharpest pods or branches of the NP. Although it is difficult to affirm that the A and B modes are not the same one because the spatial resolution for EELS studies achieved has been of 0.18 eV, and they are closer than this limit, they are the most intense spectrum determined, and there are few differences in their abundance maps. In fact, the A-mode at 0.8 eV is localized at the sharp tip growth from the main one, while the B-mode includes all the surface and surroundings of that area in the NP. The C-mode at 1.1 eV is highly localized at the second longer tip emerging from the core. The D-mode at 1.4 eV is mostly localized at the pointiest and shortest pod of the NP. To conclude with the less energetic modes, the last E-mode at 1.8 eV appears at different points of these last three sharp spikes

corresponding to A to D modes. The trend in the optical response of this kind of NPs is the same reported for nanostars: the longitudinal modes are localized at the tips of the pods growing from the core, and below 1.8 eV. Moreover, it has been reported the increase of the energy of the mode with the decrease in the length of the pod, as observed in this case [10, 48]. These are the less energetic plasmonic modes and they are hardly dependent of the size and shape of the NP, but independent from the composition of it.

The last two modes above 2.0 eV are reported in all plasmonic Au-NPs and related studies as transversal dipolar modes due to the gold core. They appear at different points but covering all the NP surface. In fact, it seems that the trend is to be complementary, so any region of the surface is excluded from these two modes. Note that there is a contribution of the D and E-modes to the F-mode at 2.1 eV, but it is negligible in front of the main peak. In the G-mode there are two important contribution by C and D-modes. On the one hand, it is proved that the C-mode is present in the NP, and in the other hand, it is difficult to discern between these modes specially in the interstitial voids between surfaces. In addition, note that this last mode does not decay to zero probably because of the same carbon peak than in spheroidal anisotropically branched NP commented above. Finally, the NPs is deposited and sustained on a carbon material as can be observed in the *Figure 5f*, so probably there are plasmonic modes unidentified corresponding to these pods used as supports totally shadowed by the carbon signal that is not included in the low-loss region studied.

6.4. Dendritic nanostructures

Finally, we will present the results of the most complex nanoparticles that we have studied, which are these dendritic nanostructures: NP-I and NP-II in yellow and purple dashed-line rectangles in *Figures 5g* and *5h*, respectively. These are a kind of arms from 100 nm to 1 μm long coming out from a core. Different areas of interesting shapes have been chosen to run the plasmonic analysis. Although the size of one duplicate the other one's, it is intuitive to think that they will present similar plasmonic modes because they differ only in one of the three main factors affecting the plasmonic response (composition, size, and shape). Otherwise, if they present different response, it may be attributable to the so-mentioned size factor. However, as in the latter case, their irregular shape may prevent the assignation of the modes with the order of the polar modes. The results are presented in *Figure 10* (NP-I) and *Figure 11* (NP-II) below.

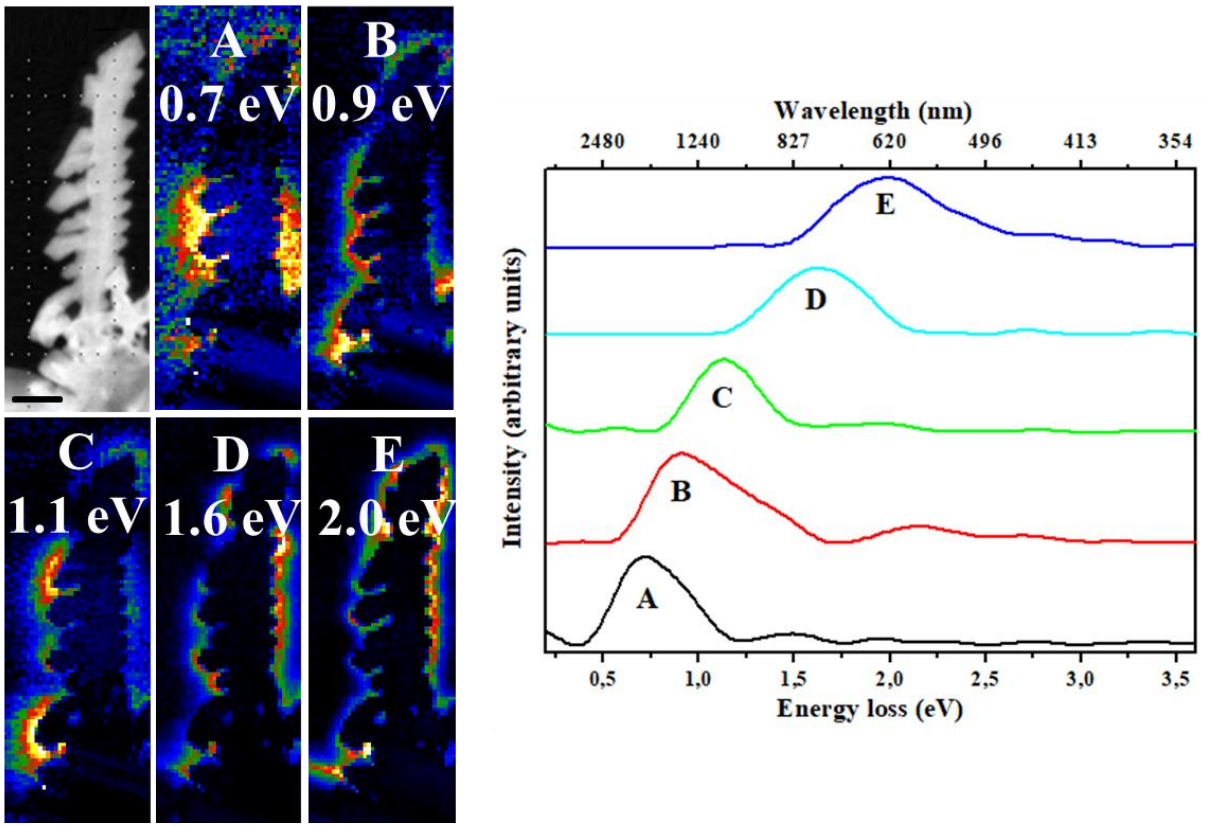

***Figure 10**. Plasmonic features of NP-I Au-nanostructure. (a) HAADF-STEM micrographs abundance maps of the components at the specified low-loss region energy (A to E). (b) Spectra of the different plasmonic responses. Black scale bar is of 50 nm.*

Five (A to E) different plasmonic modes have been identified for NP-I dendritic Au-based nanostructure in the range 0.7-2.0 eV, coinciding with the previous studies presented in this work. These modes can be classified into longitudinal polar ones (A to D) and transversal one (E) as they are dependent of the size and shape, and of the composition, respectively. Regarding the first ones, it can be observed that the less energetic polar modes are highly localized on the longest and sharpest spikes emerging from the core. This is that, the A-mode at 0.7 eV is localized on the central part of the dendritic nanostructure where the sharpest and longest spikes are, and on the tip of the nanostructure, while B-mode at 0.9 eV is localized at almost the same region, but only on the longer ones (see right side of the B-mode map in *Figure 10*). The other longitudinal modes follow the same tendency: C-mode at 1.1 eV is localized on the longer but rounded or even flat spikes on the NP-I, but not on the sharpest ones, while the more energetic D-mode at 1.6 eV appears at the shortest spikes on the nanoobject. It is not the same case as in multipods branched irregular nanostructures, but it could be a similarity between the spikes in this case and the pods in the latter, being the high energetic signal localized at the shortest spikes/pods, regarding references [10, 48]. Finally, the E-mode at 2.0 eV is the transversal mode but red-shifted due to the size and shape of the NP.

Note that in this case, the contribution of the most energetic responses to the less energetic ones can be observed in the spectra. The two clearer examples of that are the A and B-modes, that present a shoulder due to B, and C and D contributions, respectively. Other interesting signals are the one at ~2.1 eV in the B-mode that may be a contribution of the transversal mode since it more energetic than 2.0 eV, and the kind of periodicity of the A-mode but decreasing significantly the intensity of the peaks. Again, the explanation for this issue is the higher absorption and scattering cross-section at those frequencies, combined with the high localization of the mode on a tip, leading to a higher intensity. Moreover, it may be a spatial overlapping of the responses due to the complex and irregular structure of the NPs, making the difference with last examples.

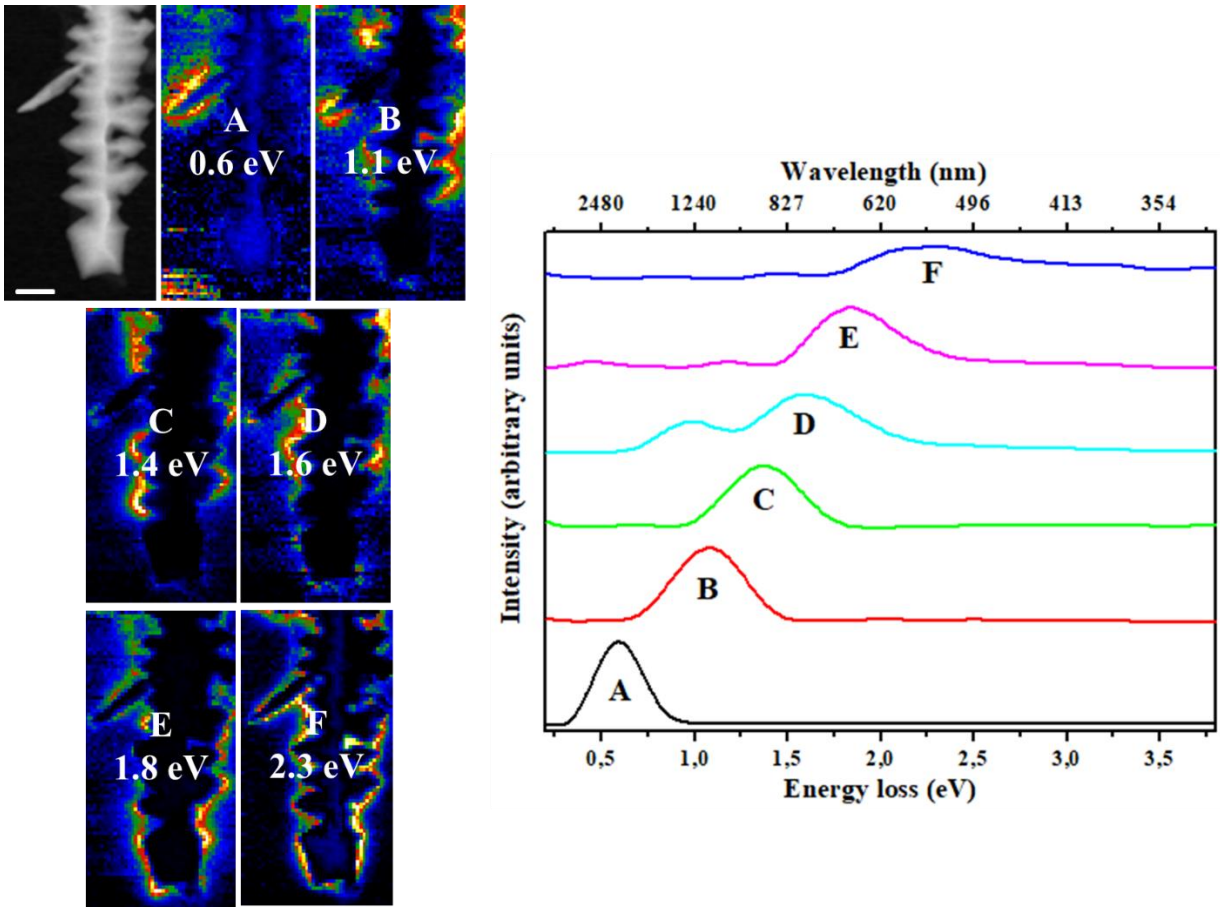

Figure 11. *Plasmonic features of NP-II Au-nanostructure. (a) HAADF-STEM micrographs abundance maps of the components at the specified low-loss region energy (A to F). (b) Spectra of the different plasmonic responses. White scale bar is of 100 nm.*

In the NP-II analysis, the optical response is really like the NP-I, but with an extra plasmonic mode, and some peak shifts attributable probably to the different size. However, note that there are six modes: five (A to E) assigned as longitudinal modes, so highly dependent of the size and shape, and one (F) transversal mode. It is easy to correlate the longitudinal modes between these two samples considering the blue shift of the latter due to its bigger size. This correlation

is: NP-I (A-0.7 eV, B-0.9 eV, C-1.1 eV and D-1.4 eV) to NP-II (A-0.6 eV, B-1.1 eV, C-1.4 eV, D-1.6 eV; being the only difference the less energetic mode in which the sharpest and longest spike of these two samples is at NP-II (A-mode). Thus, following the same line than in nanostars and NP-I, the A mode is highly localized at the sharpest and longest part of the nanoobject, while with the increasing energy, the modes are localized first on the sharpest but shortest regions (B-mode at 1.1 eV), and then on the rounded, flat and shortest regions of the nanostructure (C-mode at 1.4 eV and D-mode at 1.6 eV). Saving these similarities, the E-mode at 1.8 eV in this case, is assigned to a longitudinal mode, as commented in previous nanostructures, but it is not present in the NP-I case. Probably, the reason for that is the different size of the NPs. In fact, similar high-energy modes have been reported as size-dependent in NPs around 100 nm, as in the case of bipyramidal Au-nanostructures [3]. Finally, there is the so-known transversal, F-mode at 2.3 eV appearing in all the region.

7. Conclusions and perspectives

Low-loss EELS studies have been developed to analyze the plasmonic response of gold-based NPs with different shape and size. Systematic and detailed data analyses have been carried out in order to isolate and discriminate the different plasmonic modes. On the one hand, plasmonic modes below 1.0 eV have been identified in all the studied samples, despite the difficulties related with the subtraction of the zero-loss peak. On the other hand, we have identified highly localized surface modes related with the size and shape of the NPs following a line that can be summarized as follows: the low energy modes are related with sharp regions (around 1.0 eV) while high energy modes are related with the most rounded and flatter regions of the NPs (between 1.5 and 2.0 eV). Moreover, volume, composition-related modes have been identified in all samples, according with the theory, at higher energy values (e.g. 2.1-2.4 eV for gold and 3.0 eV for silver).

The most detailed analysis has been extracted from the arrowhead-type nanoobject, with a good matching with referenced studied on bipyramidal gold nanostructures, probably due to its regular, symmetric shape. Other interesting common features have been found between multipod branched irregular and other branched reported nanoobjects as nanostars. This fact together with the plasmonic modes identified in the other more complex samples show the opportunities to design and synthetize different sized and shaped-NPs to tune the plasmonic response for application in different nanotechnological areas as sensing and catalysis.

8. References

[1] P. Zijlstra, J. W. M. Chon y M. Gu, «Five-dimensional optical recording mediated by surface plasmons in gold nanorods,» *Nature,* vol. 459, pp. 410-413, 2009.

[2] A. J. Haes, S. Zou, G. C. Schatz y R. P. Van Duyne, «A nanoscale optical biosensor: the long range distance dependence of the localized surface plasmon resonance of noble metal nanoparticles,» *The Journal of Physical Chemistry B,* vol. 108, nº 1, pp. 109-16, 2004.

[3] R. Arenal, L. Henrard, L. Roiban, O. Ersen, J. Burgin y M. Treguer-Delapierre, «Local plasmonic studies on individual core-shell gold-silver and pure gold nano-bipyramids,» *The Journal of Physical Chemistry C,* vol. 118, pp. 25643-50, 2014.

[4] M. Prieto, R. Arenal, L. Henrard, L. Gomez, V. Sebastian y M. Arruebo, «Morphological tunability of the plasmonic response: from hollow gold nanoparticles to gold nanorings,» *The Journal of Physical Chemistry C,* vol. 118, nº 49, pp. 28804-11, 2014.

[5] V. Iberi, N. Mirsaleh-Kohan y J. P. Camden, «Understanding plasmonic properties in metallic nanostructures by correlating photonics and electronic excitations,» *The Journal of Physical Chemistry Letters,* vol. 4, pp. 1070-78, 2013.

[6] O. Benson, «Assembly of hybrid photonics architectures from nanophotonics constituents,» *Nature,* vol. 480, pp. 193-99, 2011.

[7] H. Choi, S.-J. Ko, Y. Choi, P. Joo, T. Kim, B. R. Lee, J.-W. Jung, H. J. Choi, M. Cha, J.-R. Jeong, I.-W. Hwang, M. H. Song, B.-S. Kim y J. Y. Kim, «Versatile surface plasmon resonance of carbon-dot-supported silver nanoparticles in polymer optoelectronic devices,» *Nature Photonics,* vol. 7, pp. 732-38, 2013.

[8] A. Genç, J. Patarroyo, J. Sancho-Parramon, R. Arenal, M. Duchamp, E. E. González, L. Henrard, N. G. Bastús, R. E. Dunin-Borkowski, V. F. Puntes y J. Arbiol, «Tuning the plasmonic response up: hollow cuboid metal nanostructures,» *ACS Photonics,* vol. 3, pp. 770-79, 2016.

[9] L. He, Y. Liu, J. Liu, Y. Xiong, J. Zheng, Y. Liu y Z. Tang, «Core-shell noble-metal@metal-organic-framework nanoparticles with highly selective sensing property,» *Angewandte Chemie International Edition,* vol. 52, nº 13, pp. 3741-45, 2013.

[10] J. Morla-Folch, L. Guerrini, N. Pazos-Pérez, R. Arenal y A. Álvarez-Puebla, «Synthesis and optical properties of homogeneous nanoshurikens,» *ACS Photonics,* vol. 1, pp. 1237-44, 2014.

[11] M. Grzelczak, A. Sánchez-Iglesias, H. H. Mezerji, S. Bals, J. Pérez-Yuste y L. Liz-Marzán, «Steric hindrance induces crosslike self-assembly of gold nanodumbbells,» *Nano Letters,* vol. 12, nº 8, pp. 4380-84, 2012.

[12] S. K. Gray, «Theory and modeling of plasmonic structures,» *The Journal of Physical Chemistry C,* vol. 117, pp. 1983-94, 2013.

[13] V. Myroshnychenko, J. Rodríguez-Fernández, I. Pastoriza-Santos, A. M. Funston, C. Novo, P. Mulvaney, L. M. Liz-Marzán y F. J. García de Abajo, «Modelling the optical response of gold nanoparticles,» *Chemical Society Reviews,* vol. 37, nº 9, pp. 1792-805, 2008.

[14] X. Huang y M. A. El-Sayed, «Gold nanoparticles: optical properties and implementations in cancer diagnosis and photothermal therapy,» *Journal od Advanced Research,* vol. 1, pp. 13-28, 2010.

[15] P. K. Jain, X. Huang, I. H. El-Sayed y M. A. El-Sayed, «Review of some interesting surface plasmon resonance-enhanced properties of noble metal nanoparticles and their applications to biosystems,» *Plasmonics,* vol. 2, pp. 107-18, 2007.

[16] J. Kneipp, H. Kneipp y K. Kneip, «SERS- a single-molecule and nanoscale tool for bioanalytics,» *Chemical Society Reviews,* vol. 37, pp. 1052-60, 2008.

[17] J. Nelayah, M. Kociak, O. Stéphan, F. J. García de Abajo, M. Tencé, L. Henrard, D. Taverna, I. Pastoriza-Santos, L. M. Liz-Marzán y C. Colliex, «Mapping surface plasmon on a single metallic nanoparticle,» *Nature Physics,* vol. 3, pp. 348-53, 2007.

[18] A. L. Koh, K. Bao, I. Khan, W. E. Smith, G. Kothleitner, P. Nordlander, S. A. Maier y D. W. McComb, «Electron energy-loss spectroscopy (EELS) of surface plasmons in single silver nanoparticles and dimers: influence of beam damage and mapping of dark modes,» *ACS Nano,* vol. 3, nº 10, pp. 3015-22, 2009.

[19] G. Mie, «Beiträge zur Optik trüber Medien, speaiell kolloidales Metallösungen,» *Annalen der Physik,* vol. 25, nº 377, 1908.

[20] R. B. M. Schasfoort y A. J. Tudos, Handbook of Surface Plasmon Resonance, Cambridge, UK: The Royal Society of Chemistry, 2008.

[21] L. J. Mendoza, D. Muñetón, D. C. Schinca y L. B. Scaffardi, «Determination of plasma frequency, damping constant, and size distribution from the complex dielectric function of noble metal nanoparticles,» *Journal of applied physics,* vol. 116, nº 233105, pp. 1-8, 2014.

[22] S. A. Maier, Plasmonics. Fundamentals and Applications., Bath, UK: Springer, 2007.

[23] U. Kreibig y M. Vollmer, Optical Properties of Metal Clusters, New York, US: Springer, 1995.

[24] C. Cherqui, N. Thakkar, G. Li, J. P. Camden y D. J. Masiello, «Characterizing localized surface plasmons using electron energy-loss spectroscopy,» *Annual Reviews of Physical Chemiestry,* vol. 67, pp. 331-357, 2016.

[25] E. Ruska, «The development of the electron microscope and of electron microscopy,» *Reviews of Modern Physics,* vol. 59, nº 3, p. 627, 1987.

[26] M. Kociak, O. Stéphan, A. Gloter, L. Zagonel, L. Tizei, M. Tencé, K. March, D. Blazit, Z. Mahfoud, A. Losquin, S. Meuret y C. Colliex, «Seeing and measuring in colours: Electron microscopy and spectroscopies applied to nano-optics,» *Comptes Rendus Physique,* vol. 15, nº 2-3, pp. 158-75, 2014.

[27] D. B. Williams y C. Carter, The Transmission Electron Microscope, Boston, US: Springer, 1996.

[28] L. Francis, A. Mayoral y R. Arenal, Advanced Transmission Electron Microscopy. Applications to Nanomaterials, Switzerland: Springer, 2015.

[29] M. Kociak y O. Stéphan, «Mapping plasmons at the nanometer scale in an electron microscope,» *Chemistry Society Reviews,* vol. 43, nº 1, pp. 3865-83, 2014.

[30] C. Kittel, Introduction to Solid State Physics, Nwe York, US: John Wiley & Sons, Inc., 1996.

[31] G. Ruthermann, «Diskrete energieverluste schneller elecktronen in festkörpern,» *Naturwissenschaften,* vol. 29, nº 648, 1941.

[32] D. Bohm y D. Pines, «A collective description of electron interactions: II. Collective vs individual particle aspects of the interactions,» *Physics Reviews,* vol. 85, pp. 338-53, 1952.

[33] F. Fujimoto y K.-I. Komaki, «Plasma oscillations excited by a fast electron in a metallic particle,» *Journal of Physics Society of Japan,* vol. 25, pp. 1679-87, 1968.

[34] J. Crowell y R. Richie, «Radiative decay of Coulomb-stimulated plasmons in spheres,» *Physics Reviews,* vol. 172, pp. 436-40, 1968.

[35] T. Kokkinakis y K. Alexopoulos, «Observation of radiative decay of surface plasmon in small silver particles,» *Physics Review Letters,* vol. 28, pp. 1632-34, 1972.

[36] Z. Wang y J. Cowley, «Surface plasmon excitation for supported metal partciles,» *Journal of Microscopy,* vol. 21, pp. 77-93, 1987.

[37] O. Nicoletti, F. de la Peña, R. K. Leary, D. J. Holland, C. Ducati y P. A. Midgley, «Three-dimensional imaging of localized surface plasmon resonances of metal nanoparticles,» *Nature,* vol. 502, pp. 80-4, 2013.

[38] C. Jeanguillaume y C. Colliex, «Spectrum-image: The next step in EELS digital acquisition and processing,» *Ultramicoscopy,* vol. 28, nº 1-4, pp. 252-7, 1989.

[39] R. Arenal, F. De la Pena, O. Stephan, M. Walls, M. Tence, A. Loiseau y C. Colliex, «Extending the analysis of EELS spectrum-imaging data, from elemental to bond mapping in complex nanostructures,» *Ultramicroscopy,* vol. 109, nº 1, pp. 32-8, 2008.

[40] R. F. Egerton, Electron energy-loss spectroscopy in electron microscope, Switzerland: Springer, 2011.

[41] K. Pearson, «On lines and planes of closest fit to systems of points in space,» *The London, Edinburgh, and Dublin Philosophical Magazine and Journal of Science,* vol. 2, nº 11, pp. 559-72, 1901.

[42] P. Trebbia y N. Bonnet, «EELS elemental mapping with unconventional methods I. Theoretical basis: Image analysis with multivariate statistics and entropy concepts,» *Ultramicroscopy,* vol. 111, nº 2, pp. 165-78, 1990.

[43] N. Bonnet, N. Brun y C. Colliex, «Extracting information from sequences of spatially resolved EELS spectra using multivariate statistical analysis,» *Ultramicroscopy,* vol. 77, nº 3-4, pp. 97-112, 1999.

[44] M. Pelaez-Fernández, C. P. Ewels y R. Arenal, *Optoelectronic properties and in-situ transformations of 1D and 2D materials studied by transmission electron microscopy,* U. Zaragoza: PhD Thesis (In preparation), 2020.

[45] M. C. Ortega Liebana, *Light-emitting carbon nanodots synthesis and development of novel applications PhD Thesis,* U. Zaragoza: PhD Thesis, 2018.

[46] S. J. Barrow, D. Rossouw, A. M. Funston, G. A. Botton y P. Mulvaney, «Mapping bright and dark modes in gold nanoparticle chains using electron energy loss spectroscopy,» *Nano Letters,* vol. 14, pp. 3799-808, 2014.

[47] M. Bosman, V. J. Keast, M. Watanabe, A. I. Maaroof y M. B. Cortie, «Mapping surface plasmons at the nanometre scale with an electron beam,» *Nanotechnology,* vol. 18, pp. 165505-10, 2007.

[48] S. Mazzuco, O. Stéphan, C. Colliex, I. Pastoriza-Santos, L. M. Liz-Marzán, J. García de Abajo y M. Kociak, «Spatially resolved measurements of plasmonic eigenstates in complex-shaped, asymmetric nanoparticles: gold nanostars,» *The European Physical Journal Applied Physics,* vol. 54, nº 33512, pp. 1-9, 2011.

[49] V. Garcia y M. Bibes, «Ferroelectric tunnel junctions for information storage and processing,» *Nature communications,* vol. 5, nº 4289, 2014.

[50] R. Senga, H.-P. Komsa, Z. Liu, K. Hirose-Takai, A. V. Krasheninnikov y K. Suenaga, «Atomic structure and dynamic behaviour of truly one-dimensional ionic chains inside carbon nanotubes,» *Nature Materials,* vol. 11, nº 13, pp. 1050-1054, 2014.

[51] A. Eljarrat, S. Estradé y F. Peiró, «Chapter 2: Low-loss EELS methods,» de *Advances in Imaging and Electron Physics,* London, UK, Elsevier Inc., 2019, pp. 49-77.